Ceramics

CrossMark

Lamellar and bundled domain rotations in barium titanate

Jane A. Howell[1], Mark D. Vaudin[1], Lawrence H. Friedman[1], and Robert F. Cook[1,*]

[1] *Materials Measurement Science Division, National Institute of Standards and Technology, Gaithersburg, MD 20899, USA*

ABSTRACT

Cross-correlation of electron backscatter diffraction patterns has been used to generate rotation maps of single crystals of tetragonal barium titanate (BaTiO$_3$) containing multiple lamellae and bundles of $\approx$ 90° domains. Rotation measurement angular resolutions of 0.1 mrad (0.006°) and spatial resolutions of 30 nm are demonstrated on structures with approximately 1 μm domains extending over 10s of μm. The material orientations demonstrated considerable microstructural dependence: *c* domains, with polarization perpendicular to a free surface, exhibited little within-domain rotation variation while *a*-domains, with polarization parallel to the surface, exhibited considerable within-domain variation, particularly in the larger lamellar domain structure. In both lamellar and bundled structures, the maximum *a*–*c* between-domain rotation was approximately equal to the value $\theta_r \approx 0.63°$ (11 mrad) predicted by a rigid rotation of tetragonal BaTiO$_3$ unit cells across the domain boundary. However, in both structures there was gradual variation in rotation throughout, especially adjacent to domain boundaries, suggesting that a rigid rotation model predicts too abrupt a unit cell and polarization rotation. A new BaTiO$_3$ compound defect was deduced through identification of a double integral surface rotation $2\theta_r$. The double rotation is indicative of a low-angle grain boundary terminating at a surface by a confined 90° domain.

Introduction

Two previous works [1, 2] used electron backscatter diffraction (EBSD) techniques to map the variations of stress and strain in multi-domain structures of barium titanate (BaTiO$_3$). A major goal of these works was to address the practical concern of *mechanical reliability* of BaTiO$_3$-containing multilayer ceramic capacitors (MLCCs). The goal was addressed through the development of methods to map residual stresses and strains in BaTiO$_3$ arising from the MLCC manufacturing process. Such residual stresses and strains develop as a MLCC is cooled from the manufacturing sintering temperature [3], causing BaTiO$_3$ to pass through a cubic-to-tetragonal, and associated paraelectric-to-ferroelectric, phase transformation at about 120 °C [4]. At room temperature in its undeformed state, BaTiO$_3$ is tetragonal, with the unit cell

Address correspondence to E-mail: robert.cook@nist.gov

c axis about 1.1% longer relative to two equivalent *a* axes that are perpendicular to the *c* axis and each other. The *c* axis is also the direction of unit-cell ferroelectric polarization [5]. In a bulk ferroelectric material, regions of invariant electrical polarization are termed domains and thus in BaTiO$_3$ domains are also regions of invariant *c* axis orientation. Domains develop and change configuration in a component to minimize total electrostatic and elastostatic energy [6, 7]. On cooling through the cubic-to-tetragonal phase transition temperature in BaTiO$_3$, strains develop between differently oriented domains. Hence, if transformational compatibility is maintained (no cracks, no voids), reaction stresses develop within and between domains and measurement of these stresses and strains was the focus of the previous works [1, 2]. Transformational compatibility between differently oriented domains is also achieved by rotations within and between domains, and measurement of these rotations is the focus of the current work. The rotations contribute to the overall deformation (rotation + strain) of BaTiO$_3$ on cooling, thereby affecting both mechanical and *electrical* performances (via polarization) of MLCCs, and, as will be emphasized here, provide insight into the domain microstructures that can develop. The current work has implications for other commercially relevant ferroelectric ceramics, such as lead titanate and lead zirconate titanate (PZT), in which similarly tetragonal crystal structures couple mechanical and electrical effects [8].

To provide context, before examining rotations in detail, the strains observed in the two previous EBSD studies [1, 2] considering two different domain structures will be summarized. Schematic diagrams of the two structures, also to be studied here, are shown in Fig. 1, together with a right-handed X_1–X_2–X_3 Cartesian coordinate system. The samples containing the structures were single crystals, about 4 mm square and 1 mm thick, composed predominantly of *c*-domain material but containing some *a*-domains. In a *c* domain, the *c* axis, [001], was parallel to X_3 and perpendicular to the X_1–X_2 large sample face. In an *a*-domain, one of the *a* axes, here taken as [100], was parallel to X_3 and perpendicular to the large sample face. In both domain types, the remaining *a* axis, here taken as [010], was parallel to X_2 and could be considered as a rotation axis to alternate between the *c*- and *a*-domains. In the first domain structure [1], Fig. 1a, the *a*-domains consisted
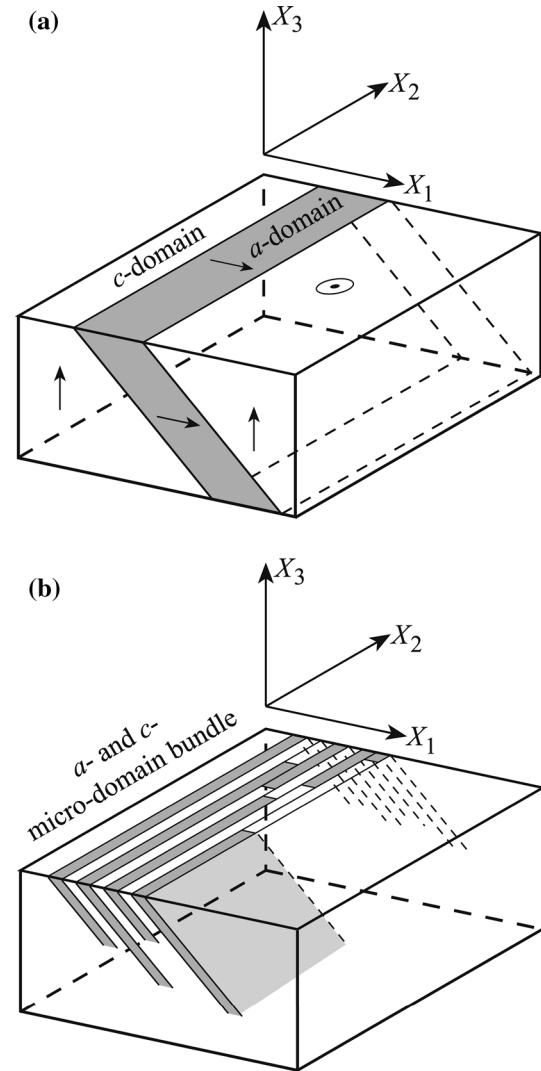
Figure 1 **a** Schematic diagram of a single lamellar *a*-domain (shown shaded) in a *c*-domain BaTiO$_3$ crystal. The polarization directions relative to the X_1–X_2–X_3 sample axes are indicated with arrows. **b** Schematic diagram of a bundle of alternating *a*- and *c*-domains imbedded in a *c*-domain BaTiO$_3$ crystal. The shading and sample axes are as in (**a**).

of long lamellae, extending in the X_2 direction across the face of the sample and about 10 μm wide in the X_1 direction at the sample surface. The *a*-domains were separated by *c*-domain lamellae of similar dimensions. Optical observations suggested that the lamellae extended through the thickness of the sample at a 45° angle to X_3 and X_1 consistent with {101} plane, *c*- to *a*-domain or vice versa, "90°" walls or boundaries [5]. In the second domain structure [2], Fig. 1b, the *a*-domains consisted of many short platelets, about 1 μm wide in the X_1 direction × 10 μm long in the X_2 direction, adjoining similarly sized *c*-

domain platelets to form mixed-domain bundles about 50 μm wide in total in the X_1 direction and extending lengthwise in the X_2 direction across the X_1–X_2 sample face. No direct information regarding the subsurface geometry of the bundles was obtained.

In both domain structures, the strain fields were dominated by two normal strain components, ε_{11} and ε_{33}, that alternated signs: In the *a*-domains, ε_{11} was negative and ε_{33} was positive; in the *c* domains, the strains were reversed, positive ε_{11} and negative ε_{33}. In both domain orientations, the magnitudes of the strains increased at the domain boundaries. Overall, the strains were consistent with the crystallographic idea that the unit cells in each domain type became more "cubic" as a domain boundary was approached to accommodate the rotated tetragonal dimensions of the unit cells in the neighboring domain—in each domain type, *a* was extended and *c* was shortened. In the case of the long lamellae, Fig. 1a, plane strain in the X_1–X_3 plane perpendicular to the lamellae, such that $\varepsilon_{22} = \varepsilon_{12} = \varepsilon_{23} = 0$, was almost ideally obeyed. In the case of the bundles, Fig. 1b, the correlation between the strain and microstructural fields was weakened, and the plane-strain condition was slightly relaxed. These observations suggested greater microstructural disorder in the bundled domains and probable subsurface termination of the platelets, as depicted in Fig. 1b. The required unit-cell rotation and associated change in surface plane orientation were considered only briefly for the lamellar domains [1].

Figure 2 shows an often-cited [5, 9–15] schematic diagram of the structure of sequential *c*–*a* and *a*–*c* domain boundaries in tetragonal BaTiO$_3$ using the same coordinate system as Fig. 1. The structure is in plane strain (in the X_1–X_3 plane of the diagram), includes strains generating a more cubic (square) structure localized at domain boundaries and incorporates rotations. The long axes of the rectangles and arrows in Fig. 2 represent the *c*-orientations and directions of polarization of unit cells within domains. The unit cells within domains are taken as rigid. The domains are separated by diagonal boundary planes and the polarizations obey the "head-to-tail" rule across the plane to minimize electrostatic energy [5]. The domain boundary region, marked by cells containing the planes represented by dashed lines, is not taken as rigid and can be described by an inhomogeneous shear strain. The change in orientation of the domains can be described by a simple rotation W about X_2. A consequence of the tetragonal BaTiO$_3$ unit-cell dimensions is that the domain rotation across the boundaries is not quite 90°; for convenience, however, *a-c* and *c-a* boundaries are often referred to as 90° boundaries [5, 10, 12–16]. (For illustration purposes, the tetragonal *c/a* distortion and hence the rotations at domain boundaries have both been exaggerated by a factor of 20 in Fig. 2.) The exterior structure of the unit cells in adjacent domains can be described by simple reflection in the boundary plane [17, 18], but not the interior polarizations of the unit cells; again, for convenience, *a*–*c* and *c*–*a* boundaries are also often referred to as twin boundaries [6, 17, 19]. The complete relationship between unit cells in adjacent domains, including interior and exterior structure, can be described by a reflection-inversion operation [18].

Figure 2 Schematic diagram of *c*–*a*–*c* domain structure with single-cell domain boundaries. The sample axes are as in Fig. 1. The arrows indicate polarization directions and the dashed lines indicate domain boundaries. The domain cells across the "kite"-shaped boundary cells are related by rigid reflection-inversion symmetry.
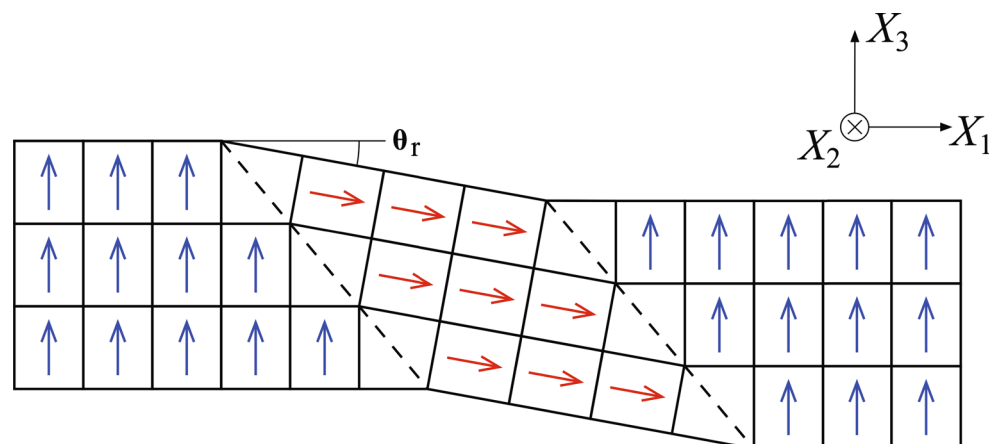
Here, attention focuses on the exterior structure alone (as sensed by EBSD) and from Fig. 2 the domain rotation angle is

$$W = \pi - 2\tan^{-1}(a/c) = \pi/2 + \theta_r \qquad (1)$$

where a and c are the unit-cell dimensions and W is positive for right-handed rotations about the positive X_2 axis as in Fig. 2 (consistent with the usual conventions [20]). The angle θ_r (defined here as a positive quantity) represents the change in orientation of material surface that was originally planar but which on transformation is related by reflection symmetry across the boundary, Fig. 2. The plane could be a near-to-free surface as in an EBSD measurement and thus a general *planar rotation angle* θ (of which θ_r is a special case) will be used here to quantify the local rotation of the material. For the rigid rotation structure shown in Fig. 2, the unit-cell dimensions of BaTiO$_3$, $a = 0.3992$ nm and $c = 0.4036$ nm [4], in Eq. (1) give $\theta_r = 0.63°$ (11 mrad) in the a-domain ($\theta = 0$ in the adjacent c domains). This angle θ is easily measured by EBSD techniques and comparable to the peak strains of $\approx 10^{-2}$ measured previously [1, 2]. The special angle θ_r is related to the tetragonal distortion by $c/a = 1 + \theta_r$ if c/a is close to 1 (Eq. (1)).

This study addresses three questions regarding domain rotation in BaTiO$_3$ raised by Fig. 2:

1. How does the change in orientation measured between domains compare with the $\theta_r = 0.63°$ value predicted by the rigid rotation structure? That is, is the predicted angle correct?
2. How does the measured variation in orientation within domains compare with the lack of variation predicted by the rigid rotation model? That is, is the domain re-orientation localized?
3. What do surface-based EBSD rotation measurements imply about subsurface domain microstructures? That is, is the modeled structure correct?

The following section describes the BaTiO$_3$ samples and EBSD measurement methods. The samples were those used previously [1, 2], as were the scanning and data collection methods. The emphasis here is on analysis of the data to obtain small length scale rotation information rather than strain information as was emphasized previously. Results are then presented as two-dimensional (2-D) rotation maps and one-dimensional (1-D) rotation and height linescans

of lamellar and bundled domain structures, as well as plots of rotation variations as a function of domain size. Discussion focuses on the materials science aspects of domain microstructures in BaTiO$_3$ that can be inferred from the measurements.

Materials and methods

Materials

Two BaTiO$_3$ single-crystal samples, predominantly c domain, used previously in strain studies [1, 2], were used for all rotation experiments. The first sample was grown by the Czochralski method and contained relatively large lamellar a-domains. The sample was in the form of a plate, approximately 4 mm $\times$ 3 mm $\times$ 1 mm thick. Prior to EBSD analysis, the sample was manually polished on one large face with a chemical–mechanical polishing solution. The second sample was grown by the top-seeded solution growth method and contained isolated 90° and 180° domains (not studied here) and bundled a and c domains. The sample was a plate, 5 mm $\times$ 5 mm $\times$ 1 mm thick and prior to EBSD was polished on one face using a colloidal silica solution. Schematic diagrams of the lamellar and bundle structures are shown in Fig. 1. The lamellae and bundles were aligned along the X_2 direction. More details, including micrographs of the sample surfaces, can be found elsewhere [1, 2]. In both cases, the polished sample surfaces were not coated before being loaded into a field emission scanning electron microscope (SEM) (Hitachi S4700 FESEM, Hitachi High-Tech, Tokyo, Japan) for EBSD analysis.

Orientation analysis

Four separate regions of each of the lamellar and bundled domain structures were examined by EBSD, and rotation analysis was performed as described below. No significant differences between any of the regions for either domain type were observed and, except where noted, detailed results for a single region for each type are reported. High-resolution EBSD patterns (EBSPs) were recorded within each region with the sample tilted at 70° to the incident electron beam using an accelerating voltage of 20 kV and a beam current of $\approx$ 2 nA. EBSD is a surface-sensitive measurement technique; an upper bound

for the escape depth of the electrons producing the EBSPs is 40 nm. Typical 2-D EBSD maps of the $BaTiO_3$ crystals were composed of at least three, parallel, 1-D linescans in the X_1 direction, consisting of at least 200 individual EBSPs. The separation between EBSPs in the X_1-direction was 0.5 µm for the large lamellar domains and 0.03 µm to 0.2 µm for the smaller domain bundles. The separation in the X_2-direction between adjacent linescans was 5 µm for the lamellar domains and 0.5 µm for the domain bundles. Each EBSP consisted of an image of 1344×1024 pixels; no binning was applied to the EBSPs, which were recorded at high gain with automatic and static background subtraction. Each EBSP was collected in approximately 1 s.

EBSPs, consisting of Kikuchi band patterns, were (1) indexed to obtain domain orientations relative to the SEM axes and thus the sample X_1–X_2–X_3 axes and (2) cross-correlated to obtain components of the rotation tensor relative to c-domain reference points within the scanned regions. The EBSPs were of sufficient quality that indexing and cross-correlation could be performed at all scan points. The obtained orientation and rotation maps were internally consistent; no filtering or censoring was applied. Example EBSD patterns are given in [1]. Each EBSP was indexed to obtain crystal orientation using Oxford HKL Flamenco software (version 5.0.9.1, Oxford Instruments, Abingdon, UK). Kikuchi band detection was determined with a resolution of the Hough space of 125, using the band edges from a circular region centered on the middle of the EBSP with a radius of 511 pixels. Indexing was determined from the automatic detection of five to six bands and provided the local orientation of the tetragonal a–a–c crystal axes relative to the X_1–X_2–X_3 sample axes in terms of SEM Euler angles. A local crystal orientation in the sample was regarded as part of a c-domain if the (c, X_3) angle was close to 0, and as part of an a-domain if the (a, X_3) angle was close to 0. In practice, an (a, X_2) angle was always close to 0, such that the transformation from a c-domain to an a-domain (or reverse) was accomplished by a near $\pm 90°$ rotation about X_2.

Rotation analysis

Entire maps (600–2250 EBSPs) were analyzed for rotation using two methods: (i) Euler angles used in the automated pattern indexing, and (ii) cross-correlation of the EBSPs (CrossCourt 3.0, BLG

Productions, Bristol, UK). In both cases, a single reference pattern was used in each dataset from the center of a c-domain (domains were determined from the orientation analysis). Reference patterns were assigned (by definition) zero rotation; all rotations θ are thus relative to these locations. Rotations were determined from analysis of 20 regions of interest (256×256 pixels) from each EBSP [21]. Cross-correlation determines eight (out of nine) independent components of the local distortion tensor $A_{ij}(\boldsymbol{x}) = \partial u_i / \partial x_j$, to give the traceless distortion tensor $\tilde{A}_{ij}$ at each location $\boldsymbol{x}$. The off-diagonal components of the traceless distortion tensor are identical to those of the full (nine-component) distortion tensor, that is $A_{ij} = \tilde{A}_{ij}, i \neq j$. The distortion tensor can be split into symmetric and antisymmetric parts:

$$A_{ij} = (A_{ij} + A_{ji})/2 + (A_{ij} - A_{ji})/2 \\ = \varepsilon_{ij} + \omega_{ij} \tag{2}$$

where the antisymmetric part ω_{ij} is given by

$$\omega_{ij} = \begin{bmatrix} 0 & -\omega_{21} & -\omega_{31} \\ \omega_{21} & 0 & -\omega_{32} \\ \omega_{31} & \omega_{32} & 0 \end{bmatrix}. \tag{3}$$

(Determination of the missing ninth independent distortion component of A_{ij} requires the use of the $BaTiO_3$ elastic constants and a closure condition, usually that the surface is in stress-free equilibrium such that the stress component $\sigma_{33} = 0$. Details are given elsewhere [2]. Determination of the rotation has no such requirement.) If the distortion is small, the symmetric component of A_{ij} can be interpreted as the infinitesimal strain tensor, ε_{ij}, and this has been the focus of previous work [1, 2, 21]. Moreover, ω_{ij} is interpreted as the infinitesimal *rotation* tensor. (For characteristic magnitudes for both quantities of $\approx 10^{-2}$ or less the assumptions are justified.) The tensor elements ω_{32}, ω_{31} and ω_{21} characterize rotations about X_1, X_2 and X_3, respectively. The scalar rotation W used earlier is then seen to be represented by the element ω_{13}. The scalar planar rotation angle θ, used earlier, can be generalized as a tensor θ_{ij} and describe rotations from the reference c-domain location for both c- and a-domains by setting

$$\theta_{ij} = \omega_{ij} \quad (c \text{ domain}) \tag{4a}$$

$$\theta_{ij} = \omega_{ij} - \pi/2 \quad (a \text{ domain}) \tag{4b}$$

noting that Eqs. (4a) and (4b) preserve θ_{ij} as positive for *clockwise* rotations about X_2 as in Fig. 2. The

advantage of using θ_{ij} is that it is a continuous variable of the correct scale for visualizing domain rotations within BaTiO$_3$. A further advantageous identity relates the shape of the BaTiO$_3$ sample surface to the lattice rotation. It results from: (1) the distortion components are small; (2) both a- and c-domains of BaTiO$_3$ are orthotropic (specifically tetragonal); and, (3) the free surface is parallel to a rectangular face of the orthotropic unit cell. Then,

$$\partial u_i / \partial x_j \approx -\theta_{ij}, \tag{5a}$$

taking into account that positive θ implies negative gradient (Fig. 2) and in particular, on integration,

$$u_3(x_1) = u_3(0) - \int_0^{x_1} \theta_{31}(\xi)\mathrm{d}\xi, \tag{5b}$$

where ξ is a dummy variable. Equation (5b) provides a means of estimating the surface height profile from rotation measurements similar to earlier studies of wedge indentation deformation fields [22, 23].

Results

Figure 3 shows orientation and rotation maps for lamellar (Fig. 3a) and bundled (Fig. 3b) domain regions in the BaTiO$_3$ crystals. The spatial scale for the two figures is the same, making clear that the bundled structure was much smaller than the lamellar structure. Both Figs. 3a and b consist of a top-most domain orientation (a or c) binary map (a is lighter) and three lower, color-filled θ contour rotation maps (greater θ is lighter). The domain orientation maps are those used earlier [1, 2] and the reference locations within c domains are indicated by circles. The rotation color scale for the lamellar domain contour maps extends to values slightly greater than θ_r (= 0.63°) predicted by the rigid rotation model for ideal reflection (Fig. 2). The rotation color scale maximum for the bundled domains is twice this value. Maps of other domain regions were similar.

There are two major points to note in Fig. 3. First, the rotations for both the lamellar and bundled domains are dominated by the θ_{31} rotation; the variations in the θ_{32} and θ_{21} rotations were more than an order of magnitude smaller than the θ_{31} rotation. This difference is consistent with the findings in the strain studies summarized above [1, 2]: In addition to states of plane stress in the X_1–X_2 plane as required by surface mechanical equilibrium, the deformations in both domain structures were close to plane strain in the X_1–X_3 plane perpendicular to the free surface. The lack of rotation out of this plane observed here is consistent with this finding. Second, there is strong

Figure 3 Domain orientation and rotation maps for a lamellar domain array (**a**) and a domain bundle (**b**). Both domain structures have the same length scale; the rotations for the lamellar domains are given by the upper scale and for the bundled domains by the lower scale. The locations of the assigned rotation-free reference points are indicated by the circles. The maps are ordered as in (**a**).
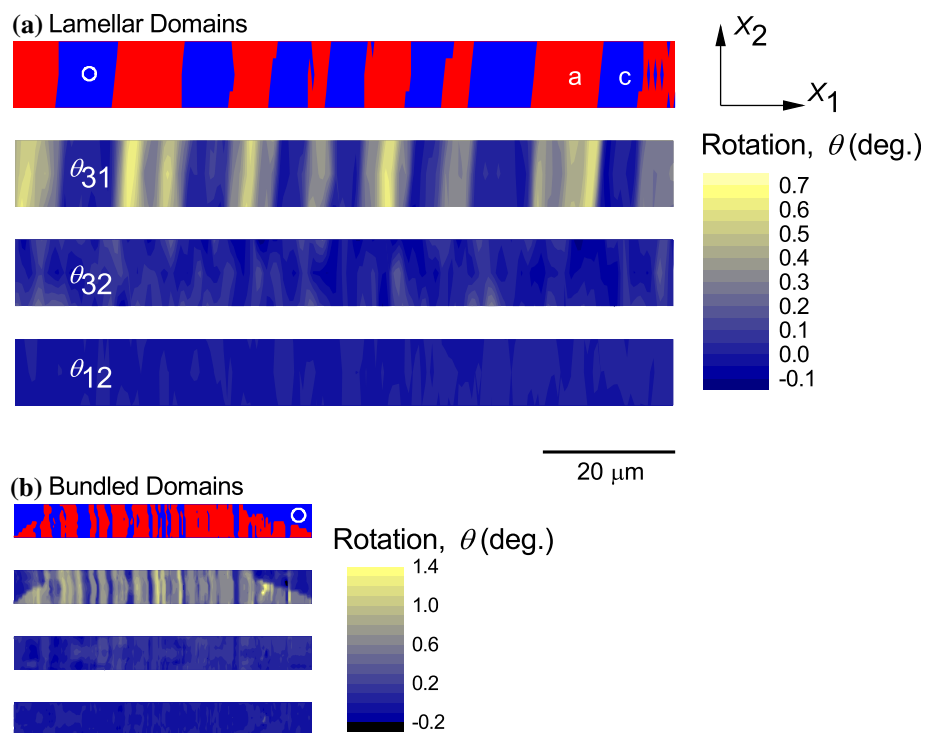
2-D spatial correlation between the rotation and the domain microstructure. In the lamellar structure, there was almost zero θ_{31} rotation in the c domains and somewhat variable rotation, peaking rarely at the rigid reflection level, in the a-domains. In the bundled domain structure, there was a similar correlation, almost zero θ_{31} rotation in the c domains but with constant rotation of approximately 0.6° in the a-domains, except as noted below. The similarity of correlation is also consistent with the strain studies in that the deformation was largely independent of the scale of the domain structure [1, 2].

Greater quantitative detail of the rotation variations is given in Fig. 4. As before, the figure is divided into two groups and the rotations are plotted as a function of the x_1 coordinate for each domain structure; Fig. 4a is of lamellar domains and Fig. 4b is of bundled domains. The upper image in each group shows the orientation maps for lamellar and bundled domains, demarcating the a and c domains as in Fig. 3 (but now using different length scales, bottom coordinates). The lower graph in each group shows
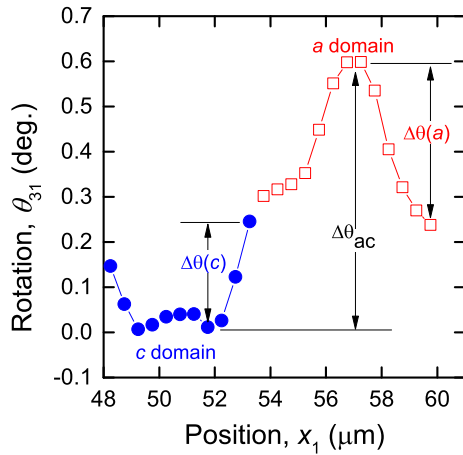

(a) Lamellar Domains
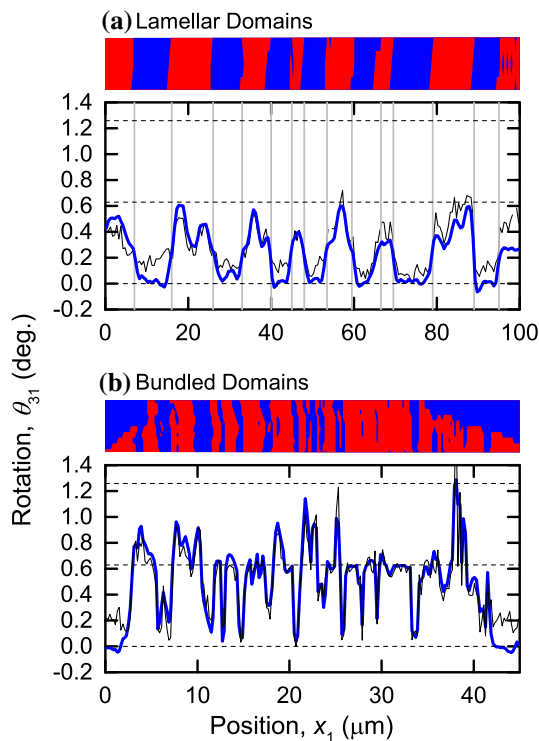
(b) Bundled Domains

Figure 4 Domain orientation and θ_{31} rotation profiles for the lamellar domains (**a**) and bundled domains (**b**) of Fig. 3. Both domain structures have the same rotation scale; the length scales for the structures are different. Bold lines are cross-correlation results; fine lines are Hough transform results.

the variations of θ_{31} (but now using the same rotation scale, left axis scales). The bold solid lines in the graphs of Fig. 4 show the variations of θ_{31} taken from single EBSD linescans; in the case of the lamellar domains from the lower edge of the map in Fig. 3 and for the bundled domains from the center of the map. The fine solid lines show the variations taken from Hough transform analyses of the same linescans and used to compose the orientation maps in Figs. 3 and 4; only the binary a or c determination was used in the orientation maps. The dashed horizontal lines in Fig. 4 indicate zero, single and double rotation values from the rigid reflection model (Fig. 2) of 0°, $\theta_{r^-} = 0.63°$ and $2\theta_r = 1.26°$, respectively.

The first point to note in Fig. 4 is the very strong agreement between the cross-correlation and Hough transform variations of θ_{31} as a function of x_1, particularly for the bundled domains. The agreement points to the accuracy of both analysis techniques and to the precision (less than 0.006°) of the more recently developed cross-correlation EBSD methods [21] that are the focus here. The second point to note is the strong correlation between the angular rotation θ_{31} and the domain designation (a or c), particularly in the case of the lamellar domains in Fig. 4a. The domain boundaries in this simple structure are indicated by the gray vertical lines. In the lamellar domains, the correlation between angular rotation and domain designation is as inferred from Fig. 3. This correlation is less obvious in the more complicated bundled domain structure in Fig. 4b (and precludes the use of lines to show domain boundaries). Nevertheless, close inspection shows some trends: The rotation in nearly all bundled a-domains is near $\theta_r = 0.63°$, more so than in the lamellar domains (which tend to peak at about 0.35°); the rotation in most bundled c domains is near 0°, not as extensively as in the lamellar domains, but there is a clear correlation; the rotation gradients at or adjacent to domain boundaries are greater in the bundled domains than in the lamellar domains (large variations in rotation over sub-micrometer distances are visible in the bundles) and are mostly restricted to within a-domains; and, important for later, the rotations in some bundled c domains approach $2\theta_r = 1.26°$.

The trends above may be generalized by examining the variations of rotation within and between domains. Figure 5 shows the variation of rotation from the lamellar domain structure at approximately

Figure 5 Expanded view of the θ_{31} rotation profile for adjacent a and c lamellar domains from Fig. 4a defining within- and between-domain rotations. The measurement uncertainty is smaller than the symbol size.

the center of Figs. 3a and 4a. The near-zero rotation within the c-domain and the larger, peaked rotation within the a-domain are clear. *Within* each domain, the maximum variation of rotation can be defined: $\Delta(a)$ in the a-domain (right side of plot) and $\Delta\theta(c)$ in the c-domain (left). *Between* each pair of neighboring domains, the maximum extent of rotation change, $\Delta\theta_{ac}$, can be defined (near center). Figure 5 illustrates these definitions (all positive magnitudes).

Figure 6 uses the above definitions. Four regions for each domain type were examined. Domain size was determined from indexing measurements such as Figs. 3a and 4a; results for similar domain sizes (surface widths) were averaged; for between-domain rotations, the a-domain dimensions were used, resulting in two data points, one for each of the left-side and right-side boundaries. The symbols represent experimental means and standard deviations. Figure 6a shows the variation of within-domain rotation as a function of domain size for lamellar structures. The solid symbols represent measurements on c domains; open symbols represent measurements on a-domains. Very little within-domain rotation occurred within c domains and most within-domain rotation for lamellae occurred in a-domains. There was a trend of increasing within-domain rotation approaching the rigid reflection θ_r value with increasing a-domain size. The bundled domain observations (not shown) were similar in that most within-domain rotation occurred in a-domains but there was no trend of within-domain rotation with domain size. Figure 6b shows the variation of
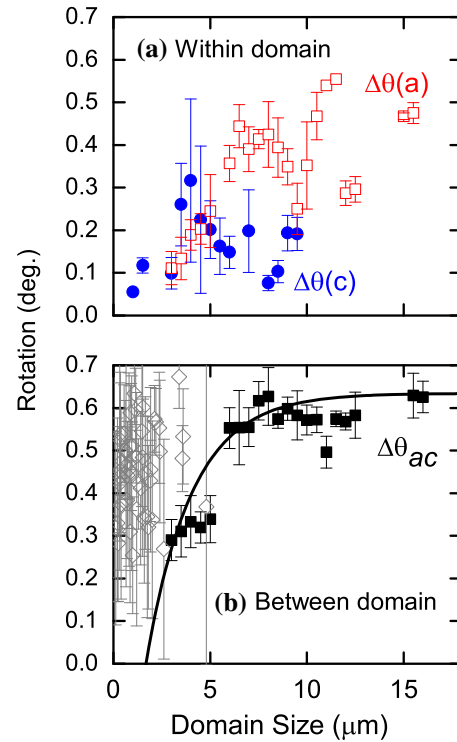
Figure 6 a Plot of within-domain rotation variation as a function of domain size for lamellar domains. **b** Plot of between-domain rotation for lamellar domains (solid symbols) and bundled domains (open symbols). The line is an empirical fit.

between-domain rotation. The solid symbols represent measurements on lamellar domains, open symbols represent measurements on bundled domains. The solid line is an empirical inverse power-law fit to the lamellar data that is constrained at large domains to the rigid reflection value of 0.63°. As the lamellar domain size decreased, the between-domain rotation changes also decreased, particularly for a-domains less than 5 µm in width. Between bundled domain pairs, the rotation changes are much larger than the values extrapolated from the lamellar domain trend, exhibit considerable variation and no real trend with domain size. These observations are consistent with *strain* changes [2], in which lamellar domains exhibited a clear trend of decreasing strain with decreasing domain size and bundled domains exhibited strains larger than the extrapolated lamellar trend and considerable variation.

Discussion

The questions posed above in the context of the rigid rotation model (Fig. 2) can now be addressed:

1. The observed *between-domain* change in orientation agrees reasonably well with the $\theta_r = 0.63°$ value predicted by the rigid rotation structure, particularly between the centers of large lamellar domains (Figs. 4a and 6a). The agreement extends less well to between-domain observations of small lamellar domains and bundled domains (Figs. 4b and 6b). The observations suggest that unit-cell dimensions (c/a) set the overall between-domain rotation structure and are consistent with previous observations on $BaTiO_3$, particularly scanning probe microscopy (SPM) measurements [11–13, 24–28] (see more below), and also transmission electron microscopy (TEM), X-ray diffraction and optical diffraction measurements [14, 29–34], and previous SPM, EBSD and TEM measurements on lead titanate [35–37] and PZT [38–41].

2. The observed *within-domain* rotation variation, extending over entire domains in the lamellar structure and predominantly adjacent to domain boundaries in the bundled structure (Figs. 3 and 4), disagrees with the lack of variation within domains predicted by the rigid rotation model (Fig. 2). Reports of observations of such variation appear to be relatively infrequent, but notably in $BaTiO_3$, observed by TEM and X-ray diffraction [42, 43] and in lead titanate and PZT, observed by EBSD and TEM [40, 41]. However, inferences and models of such variations have been made several times based on these and other observations [44–48]. The observations here in $BaTiO_3$ are the most extensive to date and suggest that within-domain unit-cell rotation variations are common and set the domain boundary structure.

3. There are significant exceptions to the answers given above for the bundled domains: Between-domain angles of $2\theta_r = 1.26°$ are sometimes observed, Fig. 4b, and within-domain invariant angles are often observed. These observations suggest that lamellar and bundled domains are perturbed from the rigid rotation model in two different ways that serve as extremes in determining the *subsurface microstructures*: one accommodating gradual rotations and one accommodating multiple rotations. These departures from the simple subsurface view of Fig. 2 are considered in turn.

The data of Figs. 3, 4, 5 and 6 describe the deformation of the material in crystal rotation space. It is possible to manipulate these data to obtain estimates of the real-space surface orientation profiles of the material. Figure 7a shows as the dashed line the approximated surface gradient variation of the lamellar material using Eq. (5a) and the EBSD data from Fig. 4. Also in Fig. 7a is the inferred height profile of the lamellar material obtained using Eq. (5b) and integrating the gradient data. The lamellar height profile data are used here in two
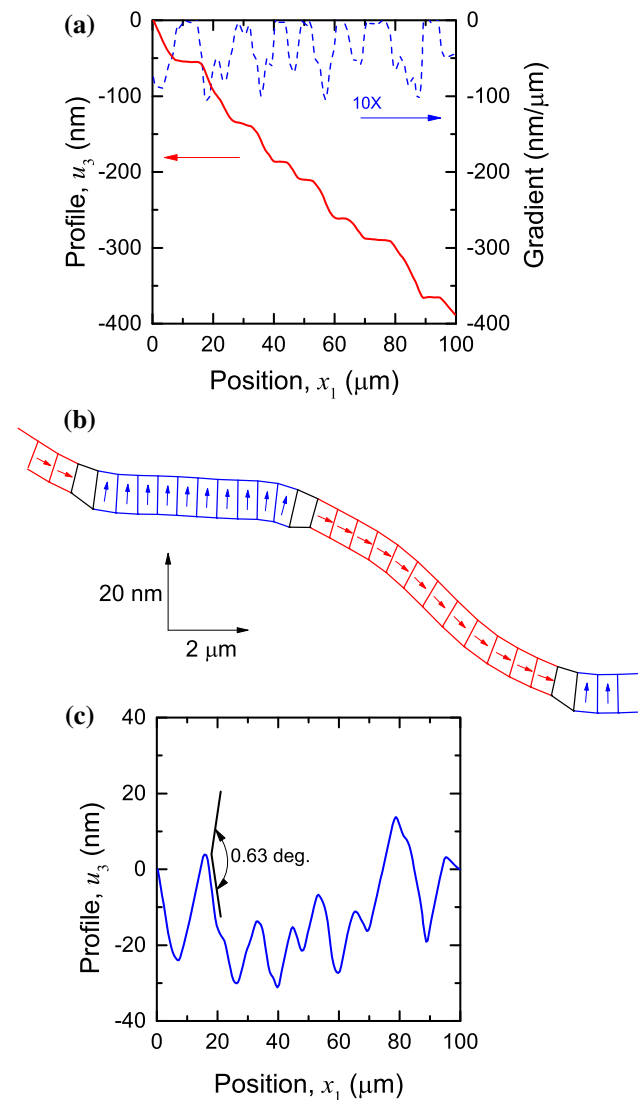
Figure 7 **a** Plots of surface gradient (dashed line) and surface profile (solid line) over a lamellar domain array. **b** Lamellar domain orientation "snake" calculated from profile information in (**a**) and index information from Fig. 3. **c** Surface profile of a lamellar domain array from (**a**) as typically observed in a SPM trace. (Note the extreme vertical exaggerations in (**b**) and (**c**)).

ways. In the first use, the profile data are combined with gradient data and the domain index binary data, Figs. 3 and 4, to generate a "snake"-like near surface visualization of the domain microstructure. Such a visualization is shown in Fig. 7b for the same 48–61 μm position range as shown in Fig. 5. The upper surface of the "snake" is the inferred surface profile taken from Fig. 7a. The lower surface was obtained by projecting the surface normals obtained from the gradient in Fig. 7a from the upper surface. The macroscopic orientation of the arrows indicates the c axis and polarization direction and was obtained from the indexing of Fig. 3. The detailed orientation of the arrows was obtained from the calculated average cell orientation. Arrows were omitted from the domain boundary cells. Note that the indicated length scales apply only to the macroscopic shape of the snake and the horizontal spacing of the cells (the sampling spacing, 0.5 μm). For illustration purposes, the vertical dimensions of the cells and thus the angular variation of the polarization have been exaggerated by a factor of 30. As noted earlier, the a-domain material exhibits much greater variation in orientation than does the c-domain material. Also, as noted earlier (Fig. 2), the a-domain and c-domain regions are separated by distorted "kite"-shaped cells: Two upward kites are visible at the edges of the profile at a–c boundaries and one downward kite is visible in the center of the profile at a c–a boundary.

In the second use, the height profile data are treated similarly to raw SPM data. In particular, the background is subtracted and the resulting height variation is enhanced (here by a factor of 1000, typical for SPM). Figure 7c shows such a manipulated profile and suggests a much rougher surface than Fig. 7a or b. The V-shaped lines in Fig. 7c indicate an included angle of 0.63° (11 mrad), the rigid reflection angle, showing that the surface is not as rough as the manipulated profile might imply. SPM provides no subsurface information, but comparison with the binary index data shows the straight sections ascending to the right are c domains and the curved sections ascending to the left are a-domains. The inferred profile of Fig. 7c is very similar qualitatively and quantitatively to direct SPM surface profile measurements of BaTiO$_3$ [12, 13, 24–28] and similarly structured PbTiO$_3$ [34, 35]: straight facets about 10 μm in length and 20 nm in height alternating in orientation by approximately 0.5° (consistent with

between-domain rotation measurements by transmission electron microscopy and X-ray and optical diffraction [14, 15, 30, 31]).

Perhaps the most significant observation, previously unreported, with implications for subsurface microstructure is the occasional $2\theta_r$ rotations observed on the surface of the bundled domain material. Figure 4 shows that such $2\theta_r$ rotations occur in c domains surrounded by a-domains of θ_r rotation (all relative to the c-domain reference of $\theta = 0$). A schematic diagram of such a rotation sequence and its likely subsurface structure is shown in Fig. 8, consistent with observations at $x_1 \approx$ 30 μm to 45 μm in Fig. 4b. In particular, the domain surface sequence proceeding left-to-right, taking the c-domain at the left of the diagram as the reference, is $c^+(0)//a^+(\theta_r)//c^-(2\theta_r)//a^+(\theta_r)//c^+(0)$, where a or c indicates the cell exterior domain index, $+$ or $-$ indicates the cell interior domain polarization, (θ) indicates the domain surface plane orientation and $//$ indicates a domain boundary. (The cell tetragonality and rotations are exaggerated by a factor of 20.) Note that once the domain indices and surface plane orientations are set by experiment, the boundary orientations, downward to the right or left, which are not observable directly by EBSD measurements, are then determined. The boundary orientations then constrain the polarization sequence, also not observable by EBSD but which must obey the "head-to-tail" rule to avoid high energy charge buildup at domain boundaries [5].

The commonly cited structure of Fig. 2 illustrates the sequence $c^+(0)//a^+(\theta_r)//c^+(0)$. For this surface sequence, the subsurface domain boundaries are both downward to the right, and as a consequence the sequence could extend and repeat many times with no boundary convergence. This is the likely lamellar structure. The left-most surface sequence of Fig. 8, $c^+(0)//a^+(\theta_r)//c^-(2\theta_r)$, however, leads to adjacent subsurface domain boundaries that are downward to the right then left, and as consequence the boundaries converge, leading to a confined a-domain. Beneath the a-domain, the two originally separated c domains converge, forming a low-angle $2\theta_r = 1.26°$ tilt grain boundary (in this case, near vertical) consisting of an array of edge dislocations [49]. As this is a covalent-ionic material and charge must be conserved, there is an "extra half plane" of unit cells. The grain boundary is also a "180°" domain boundary and could exit a sample as shown at the bottom left of the diagram. The

Figure 8 Schematic diagram of the surface and subsurface structure of a group of bundled domains, consistent with the rotation profile of Fig. 4a. A series of edge dislocations forming a low-angle grain boundary that is terminated near the surface by two converging domain boundaries enclosing a confined domain is shown at the left. The compound structure comprises a new ferroelectric defect associated with a surface rotation of $2\theta_r$.
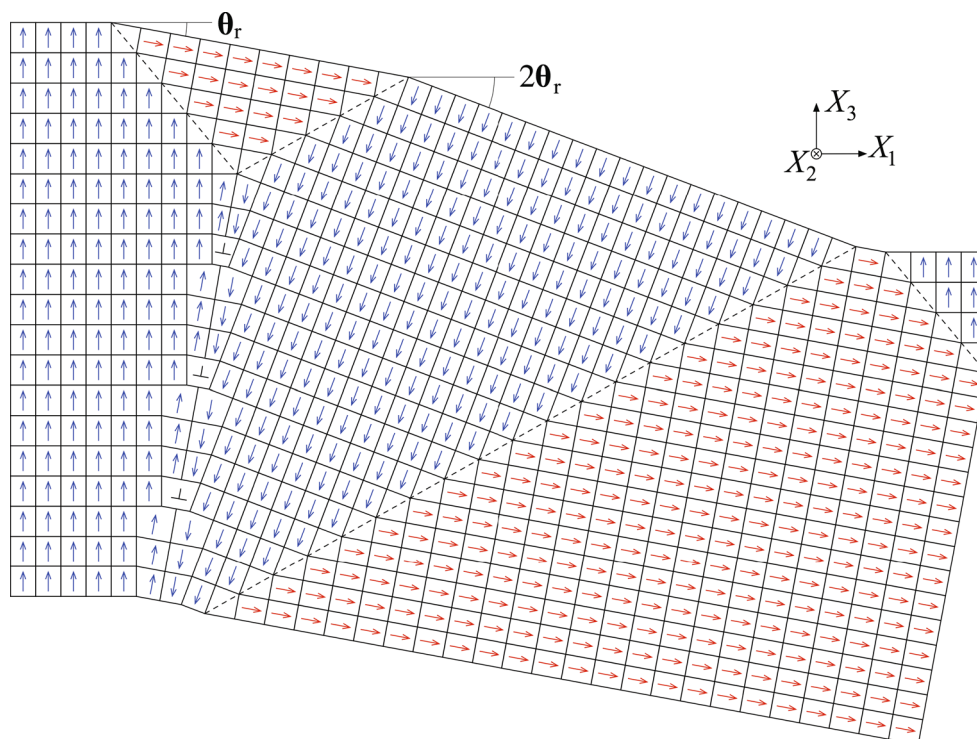
exaggerated tetragonality reduces the apparent dislocation separation by about a factor of 10: In reality, the separation is $a/(2\theta_r) \approx 0.4$ nm $\times 45 \approx 18$ nm. Similar low-angle grain boundaries consisting of arrays of edge dislocations have been observed by TEM in BaTiO$_3$ (tilts = 7.6° and 12.6°, spacings ≈ 3.0 nm and 1.8 nm) [50] and by TEM in similar strontium titanate (tilt = 0.95°, spacing ≈ 25 nm) [51], (tilt = 5°, spacing ≈ 6.3 nm) [52] and (tilt = 10°, spacing ≈ 2.4 nm) [53]. Arrays of edge dislocations have also been used in simulations of low-angle grain boundaries in both materials [54, 55]. In neither the TEM observations nor the simulations have the low-angle boundaries been associated with any other feature. Here, the observation of the $2\theta_r$ surface rotation implies the existence of a subsurface domain termination and a low-angle grain boundary. This is a new ferroelectric compound defect.

The right-most surface sequence of Fig. 8, $c^+(2\theta_r)//a^+(\theta_r)//c^-(0)$, leads to adjacent subsurface domain boundaries that are downward to the left then right, and as consequence the boundaries do not converge subsurface, leading to a gradually enlarging wedge-shaped a-domain. The $c^+(2\theta_r)//a^+(\theta_r)$ boundary extends and exits the bottom of the sample at left. The $a^+(\theta_r)//c^-(0)$ boundary extends and exits the side of the sample at right. The total c–a–c–a–

c combined sequence gives rise to a domain bundle, visible from the surface as finely divided domains. The implications for the subsurface structure are that the domain structures and the consequent strain fields can be complex and very different from the lamellae. As noted in a study of similar PZT bundled domains [56], the small domains are also localized in the X_2 dimension, as well as X_1 as illustrated, suggesting that the structure of Fig. 8 would also extend in the X_2 direction, leading to three dimensionally localized domains. Such domain structures would lead to a weakened biaxial strain field compared with the lamellae, as observed [1, 2]. Clear next steps are to assess the stability of the domain structures, taking both strain and rotation into account.

Conclusions

High-resolution EBSD is an extremely effective measurement tool for quantitative measurement of *rotation*, as well as strain, at small scales, thereby enabling complete determination of deformation behavior at the surface of complicated micro- and nanoscale structures. Rotation measurement here was demonstrated on 10-µm lamellae and < 1-µm platelet domains in BaTiO$_3$, with characteristic rotation variations of 10 mrad measured with 0.1 mrad angular

resolution and spatial pixel sizes of 30 nm to 200 nm. As with EBSD-based strain measurements, rotations were correlated with microstructure, exhibiting little variation in c domains and variations extending over several μm in a-domains in the larger lamellar structure. In the smaller bundled structure, the rotation variations were more restricted, extending over less than 1 μm. In both cases, the rotation variations were greatest adjacent to domain boundaries, and the maximum rotations were typically close to the rigid rotation domain boundary model value of 0.63° (11 mrad). The observations support the rigid rotation model as a quantitative description of the limiting angular variation between domains based on the tetragonal distortion of BaTiO$_3$. However, the observed extended rotation variations suggest that the unit-cell re-orientation at domain boundaries is not abrupt, consistent with the extended strain measurements, implying that domain boundaries in BaTiO$_3$ exhibit gradual deformation structures. The surface-based EBSD measurements were consistent with uncharged parallel 90° domain boundaries in the lamellar structure extending macroscopically through the sample. However, new observations in the bundled structure of rotations of 1.26°, about twice the rigid rotation value, implied a new type of BaTiO$_3$ defect: The measurements suggested the existence of *converging* 90° domain boundaries surrounding confined wedge-shaped surface domains terminating subsurface low-angle near-180° domain (or grain) boundaries. The new rotation observations explain the difference between the lamellar and bundled domains as not just one of scale, but of structure: The bundled domains exhibit much greater shear strain and rotation variation to accommodate subsurface constrictions that are absent in the lamellar domain structures. Extending these observations to embedded and electroded MLCC domain structures suggests that deformation consisting of both strain and rotation will be required to accommodate the additional mechanical and electrical constraints. The current work provides a firm foundation for quantifying such deformation.

Acknowledgements

References

[1] Howell JA, Vaudin MD, Cook RF (2014) Orientation, stress, and strain in an (001) barium titanate single crystal with 90 lamellar domains determined using electron backscatter diffraction. J Mater Sci 49:2213–2224. https://doi.org/10.1007/s10853-013-7915-3

[2] Howell JA, Vaudin MD, Friedman LH, Cook RF (2017) Stress and strain mapping of micro-domain bundles in barium titanate using electron backscatter diffraction. J Mater Sci 52:12608–12623. https://doi.org/10.1007/s10853-017-1355-4

[3] Pan MJ, Randall CA (2010) A brief introduction to ceramic capacitors. IEEE Electr Insul Mag 26:44–50

[4] Kwei GH, Lawson AC, Billinge SJL, Cheong SW (1993) Structures of the ferroelectric phases of barium–titanate. J Phys Chem 97:2368–2377

[5] Jona F, Shirane G (1993) Ferroelectric crystals. Dover Publications Inc, New York

[6] Arlt G (1990) Twinning in ferroelectric and ferroelastic ceramics: stress relief. J Mater Sci 25:2655–2666. https://doi.org/10.1007/BF00584864

[7] Kim S-B, Chung T-J, Kim D-Y (1993) Effect of external compressive stress on the domain configuration of barium titanate ceramics. J Eur Ceram Soc 12:147–151

[8] Haertling GH (1999) Ferroelectric ceramics: history and Technology. J Am Ceram Soc 82:797–818

[9] Hu YH, Chan HM, Wen ZX, Harmer MP (1986) Scanning electron microscopy and transmission electron microscopy of ferroelectric domains in doped BaTiO$_3$. J Am Ceram Soc 69:594–602

[10] Tsai F, Cowley JM (1993) Observation of planar defects by reflection electron microscopy. Ultramicroscopy 52:400–403

[11] Hamazaki S-I, Shimizu F, Kojima S, Takashige M (1995) AFM observation of 90 domains of BaTiO$_3$ butterfly crystals. J Phys Soc Jpn 64:3660–3663

[12] Takashige M, Hamazaki S-I, Nobutaka G, Shimizu F, Kojima S (1996) Atomic force microscope observation of ferroelectrics: barium titanate and Rochelle salt. Jpn J Appl Phys 35:5181–5184

[13] Pang GKH, Baba-Kishi KZ (1998) Characterization of butterfly single crystals of BaTiO$_3$ by atomic force, optical and

scanning electron microscopy techniques. J Phys D Appl Phys 31:2846–2853

[14] Melnichuk M, Wood LT (2003) Fraunhofer diffraction to determine the twin angle in single-crystal $BaTiO_3$. Appl Optics 32:4463–4467

[15] Yoneda Y, Kohmura Y, Suzuki Y, Hamazaki S, Takashige M (2004) X-ray diffraction topography on a $BaTiO_3$ crystal. J Phys Soc Jpn 73:1050–1053

[16] Merz WJ (1952) Domain properties in $BaTiO_3$. Phys Rev 88:421–422

[17] Oppolzer H, Schmelz H (1983) Investigation of twin lamellae in $BaTiO_3$ ceramics. J Am Ceram Soc 66:444–446

[18] Cheng S-Y, Ho N-J, Lu H-Y (2006) Transformation-induced twinning: the 90 and 180 ferroelectric domains in tetragonal barium titanate. J Am Ceram Soc 89:2177–2187

[19] Forsbergh PW (1949) Domain structures and phase transitions in barium titanate. Phys Rev 76:1187–1201

[20] Mase WE (1970) Continuum mechanics. McGraw-Hill, New York

[21] Wilkinson AJ, Meaden G, Dingley DJ (2006) High resolution mapping of strains and rotations using electron backscatter diffraction. Mater Sci Technol 22:1271–1278

[22] Vaudin MD, Stan G, Gerbig YB, Cook RF (2011) High resolution surface morphology measurements using EBSD cross-correlation techniques and AFM. Ultramicroscopy 111:1206–1213

[23] Friedman LH, Vaudin MD, Stranick SJ, Stan G, Gerbig YB, Osborn WA, Cook RF (2016) Assessing strain mapping by electron backscatter diffraction and confocal Raman microscopy using wedge-indented Si. Ultramicroscopy 163:75–86

[24] Takashige M, Hamazaki S-I, Shimizu F, Kojima S (1997) Observation of 90 domains in $BaTiO_3$ by atomic force microscopy. Ferroelectrics 196:211–214

[25] Takashige M, Hamazaki S-I, Takahashi Y, Shimizu F, Yamaguchi T (1999) Temperature dependent surface images of $BaTiO_3$ observed by atomic force microscopy. Jpn J Appl Phys 38:5686–5688

[26] Balakumar S, Xu JB, Ma JX, Ganesamoorthy S, Wilson IH (1997) Surface morphology of ferroelectric domains in $BaTiO_3$ single crystals: an atomic force microscope study. Jpn J Appl Phys 36:5566–5569

[27] Kalinin SV, Bonnell DA (2000) Effect of phase transition on the surface potential of the $BaTiO_3$ (100) surface by variable temperature scanning surface potential microscopy. J Appl Phys 87:3950–3957

[28] Nakahara H, Kaku S, Minakuchi T (2010) Observation of ferroelectric domains having atomically ordered surface in air by atomic force microscopy and piezoresponse force microscopy. Ferroelectrics 401:192–195

[29] Pramanick A, Jones JL, Tutncu G, Gjosh D, Stoica AD, An K (2012) Strain incompatibility and residual strains in ferroelectric single crystals. Sci Rep 2:929

[30] Tsai F, Cowley JM (1992) Observation of ferroelectric domain boundaries in $BaTiO_3$ single crystals by reflection electron microscopy. Ultramicroscopy 45:43–53

[31] Yoneda Y, Mizuki J-I, Kohmura Y, Suzuki Y, Hamazaki S-I, Takashige M (2004) X-ray topography on domain-controlled $BaTiO_3$ crystals. Jpn J Appl Phys 43:6821–6824

[32] Yoneda Y, Kohmura Y, Suzuki Y, Morimura R, Kojima A, Mizuki J-I (2007) Direct observation of non-strain-free style domain in $BaTiO_3$ crystal by synchrotron X-ray topography. Trans Mater Res Soc Jpn 32:31–34

[33] Potnis PR, Huber JE, Sutter JP, Hofmann F, Abbey B, Korsunsky (2010) Mapping of domain structure in barium titanate single crystals by synchrotron X-ray topography. In: Ounaies Z, Li J (ed) Behavior and mechanics of multifunctional materials and composites. Proc. SPIE 76440A-1-10

[34] El-Naggar MY, Boyd DA, Goodwin DG (2005) Characterization of highly-oriented ferroelectric $Pb_xBa_{1-x}TiO_3$ thin films grown by metalorganic chemical vapor deposition. J Mater Res 20:2969–2976

[35] Wang YG, Dec J, Kleemann W (1998) Study on surface and domain structures in $PbTiO_3$ crystals by atomic force microscopy. J Appl Phys 84:6795–6799

[36] Shilo D, Ravichandran G, Bhattacharya K (2004) Investigation of twin-wall structure at the nanometer scale using atomic force microscopy. Nat Mat 3:453–457

[37] Park BM, Chung SJ, Kim HS, Si WM, Dudley M (1997) Synchrotron white-beam X-ray topography of ferroelectric domains in a $BaTiO_3$ single crystal. Philos Mag A 75:611–620

[38] Tsai F, Khiznichenko V, Cowley JM (1992) High-resolution electron microscopy of 90 ferroelectric domain boundaries in $BaTiO_3$ and $Pb(Zr_{0.52}Ti_{0.48})O_3$. Ultramicroscopy 45:55–63

[39] Ganpule CS, Nagarajan V, Hill BK, Roytburd AL, Williams ED, Ramesh R, Alpay SP, Roelofs Waser R, Eng LM (2002) Imaging three-dimensional polarization in epitaxial polydomain ferroelectric thin films. J Appl Phys 91:1477–1481

[40] Farooq MU, Villaurrutia R, Maclaren I, Kungl H, Hoffmann MJ, Fundenberger J-J, Bouzy E (2008) Using EBSD and TEM-Kikuchi patterns to study local crystallography at the domain boundaries of lead zirconate titanate. J Microsc 230:445–454

[41] Farooq MU, Villaurrutia R, Maclaren I, Burnett TL, Comyn TP, Bell AJ, Kungl H, Hoffmann MJ (2008) Electron backscatter diffraction mapping of herringbone domain structures in tetragonal ferroelectrics. J Appl Phys 104:024111-1-8

[42] Ross FM, Kilaas R, Snoeck E, Hÿtch M, Thorel A, Normand L (1997) Quantitative analysis of displacements at 90° domain boundaries in BaTiO$_3$ and PbTiO$_3$. In: Smith DJ (ed) Materials research society symposium proceedings, vol 466, pp 245–252

[43] Holt M, Hassani Kh, Sutton M (2005) Microstructure of ferroelectric domains in BaTiO$_3$ observed via X-ray microdiffraction. Phys Rev Lett 95:085504

[44] Yakunin SI, Shakmanov VV, Spivak GV, Vasil'eva NV (1972) Microstructure of domains and domain walls in single-crystal films of barium titanate. Sov Phys Sol State 14:310–313

[45] Cao W, Cross LE (1991) Theory of tetragonal twin structures in ferroelectric perovskites with a first-order phase transition. Phys Rev B 44:5–12

[46] Zhang W, Bhattacharya K (2005) A computational model of ferroelectric domains. Part I: model formulation and domain switching. Acta Mater 53:185–198

[47] Daniels JE, Jones JL, Finlayson TR (2006) Characterization of domain structures from diffraction profiles in tetragonal ferroelastic ceramics. J Phys D Appl Phys 39:5294–5299

[48] Pramanick A, Jones JL, Tutuncu G, Ghosh D, Stoica AD, An K (2012) Strain incompatibility and residual strains in ferroelectric single crystals. Sci Rep 2:929

[49] Read WT (1953) Dislocations in Crystals. McGraw-Hill Book Company Inc, New York

[50] Igarashi M, Sato Y, Shibata N, Yamamoto T, Ikuhara Y (2006) HRTEM study of [001] low-angle tilt grain boundaries in fiber-texture BaTiO$_3$ thin films. J Mater Sci 41:5146–5150. https://doi.org/10.1007/s10853-006-0447-3

[51] Fujimoto M (1985) The structure of a migrating low-angle tilt grain boundary in strontium titanate. J Mater Sci 20:3515–3523. https://doi.org/10.1007/BF01113757

[52] Takehara K, Sato Y, Tohei T, Shibata N, Ikuhara Y (2014) Titanium enrichment and strontium depletion near edge dislocation in strontium titanate [001]/(110) low-angle tilt grain boundary. J Mater Sci 49:3962–3969. https://doi.org/10.1007/s10853-014-8034-5

[53] Gao P, Ishikawa R, Feng B, Kumamoto A, Shibata N, Ikuhara Y (2018) Atomic-scale structure relaxation, chemistry and charge distribution of dislocation cores in SrTiO$_3$. Ultramicroscopy 184:217–224

[54] Pertsev NA, Arlt G (1991) Dislocation method for calculation of internal stresses in polycrystalline ferroelectrics. Sov Phys – Sol State 33:1738-1744

[55] Imaeda M, Mizoguchi T, Sato Y, Lee H-S, Findlay SD, Shibata N, Yamamoto T, Ikuhara Y (2008) Atomic structure, electronic structure, and defect energies in [001](310)Σ5 grain boundaries in SrTiO$_3$ and BaTiO$_3$. Phys Rev B 78:245320-1-12

[56] Ivry Y, Chu DP, Durkan C (2010) Bundles of polytwins as meta-elastic domains in the thin polycrystalline simple multiferroic system PZT. Nanotechnology 21:065702-1-7